PCCP

PAPER

View Article Online
View Journal | View Issue

Cite this: *Phys. Chem. Chem. Phys.*, 2025, **27**, 12593

Aggregation-induced emission mechanism of styrene derivative: a theoretical study†

Aarzoo,[a] Kenichiro Saita,[b] Masato Kobayashi,[bc] Takao Tsuneda,*[bd] Tetsuya Taketsugu[bc] and Ram Kinkar Roy*[abc]

The aggregation-induced emission (AIE) mechanism of the fluorescent styrene derivative 4-dimethylamino-2-benzylidene malonic acid dimethyl ester (BIM) in methanol solution is theoretically investigated using spin–flip long-range corrected time-dependent density functional theory (SF-LC-TDDFT). The potential energy surfaces (PESs) for the ground (S_0) and first singlet excited (S_1) states of BIM were calculated along the rotation of the aryl main axis (α angle rotation), consistent with experimental observations. For the monomer, our findings reveal a significant reduction in oscillator strength, approaching zero at the optimized geometry in the S_1 state. As this state corresponds to a charge transfer state, it suggests that the BIM monomer operates as a twisted intramolecular charge transfer (TICT) system, undergoing quenching through α angle rotation. The restriction of TICT, and consequently the inhibition of fluorescence quenching in the aggregate state, is also investigated by extracting the coordinates of 13 monomers from the crystal structure of BIM. The α-torsional angle of the central monomer was manually rotated in both clockwise and anti-clockwise directions to assess the intramolecular restrictions within the constrained environment. This analysis reveals that even a 10° rotation of the α-torsional angle, in either direction, causes the atoms of the central monomer to come into close contact with the atoms of the neighboring monomers. These short contacts effectively inhibit the TICT process, thereby leading to aggregation-induced emission.

Received 16th December 2024,
Accepted 27th May 2025

DOI: 10.1039/d4cp04742g

rsc.li/pccp

1. Introduction

Organic dyes often exhibit luminescence quenching at high concentrations or in aggregates due to strong π–π stacking interactions between organic fluorophores. At these concentrations, the intense fluorescence, usually observed in diluted solutions, is significantly diminished or completely extinguished. This phenomenon, known as concentration quenching or aggregation-caused quenching,[1–3] limits the practical use of these dyes in solid-state applications. However, in 2001, Tang *et al.* documented an opposite phenomenon to aggregation-caused quenching, where organic fluorophores, typically non-emissive or less emissive at the molecular state, become highly emissive when aggregated. They introduced the term 'aggregation-induced emission' (AIE) to describe this behavior, with methyl-1,2,3,4,5-pentaphenylsilole being the first molecule identified to exhibit AIE.[4] Following this discovery, numerous types of AIE luminogens (AIEgens) have been developed[5] and have found successful applications in organic light-emitting diodes,[6–8] luminescent solar concentrators,[9] chemosensors,[10] and biological probes.[11] These probes are now extensively used in applications ranging from simple cell imaging to integrated theranostic platforms.[12–14]

Since the discovery of AIE, experimental and theoretical studies have focused on elucidating its mechanism. Recent studies suggest that AIE involves restriction of intramolecular rotation (RIR),[15–17] vibration (RIV)[18,19] as well as overall molecular motions.[20,21] Processes such as excited state intramolecular proton transfer (ESIPT)[22] are also being implicated in the cause of AIE. So far, the general consensus is that restricting intramolecular motions is a key mechanism behind

[a] *Dept. of Chemistry, BITS-PILANI, Pilani Campus, Rajasthan, India. E-mail: rkroy@pilani.bits-pilani.ac.in*
[b] *Department of Chemistry, Faculty of Science, Hokkaido University, N10-W8, Kita-ku, Sapporo 060-0810, Japan. E-mail: takaotsuneda@sci.hokudai.ac.jp*
[c] *Institute for Chemical Reaction Design and Discovery (WPI-ICReDD), Hokkaido University, N21-W10, Kita-ku, Sapporo 001-0020, Japan*
[d] *Graduate School of System Information, Kobe University, Japan*

† Electronic supplementary information (ESI) available: Optimized α, β, γ, and γ' angles and calculated vertical $S_0 \rightarrow S_1$ excitation energies using various functionals; $\langle S^2 \rangle$ values at S_0 and S_1 optimized geometries; Oscillator strength values, $\langle S^2 \rangle$ values, and potential energy difference between S_0 and S_1 states *vs.* torsional angle (α) at S_1-MEP; potential energy difference between S_0 and S_1 states *vs.* torsional angle (β) at S_1-MEP; potential energy difference between S_0 and S_1 states *vs.* torsional angle (α) at S_1-MEP using SF-LC-TDDFT/ωB97XD/aug-cc-pVDZ in the S_1 state; molecular orbitals of BIM monomer at the S_0 and S_1 optimum geometries; optimized α, β, γ, and γ' angles in the S_0 and S_1 states using DFT/ωB97XD/cc-pVDZ in the S_0 state and TDωB97XD/cc-pVDZ in the S_1 state; Cartesian coordinates of S_0-MIN, S_1-MIN for BIM monomer in methanol. See DOI: https://doi.org/10.1039/d4cp04742g

the enhanced emission in most AIEgens.[23,24] This is because unrestricted active rotation, vibration, or other molecular motions consume energy, leading to radiationless dissipation of exciton energy. In a molecular state, these movements promote nonradiative decay. However, when aggregates form, restricting these intramolecular motions prevents nonradiative pathways, resulting in enhanced emission. Theoretical studies on AIE have utilized Fermi's golden rule, a widely used method to calculate the nonradiative decay rate (k_{nr}) associated with the restriction of intramolecular motion.[25–27] As an alternative, the restricted access to a conical intersection (RACI) model, introduced by Blancafort and co-workers,[28] has been recently implemented to elucidate AIE in the context of the global potential energy surface (PES).[29–33] Ref. 29 details the differences and similarities between the Fermi's golden rule and RACI approaches. Conical intersection is a region where the ground and the excited states are degenerate, maximizing the probability of nonradiative internal conversion. In the RACI model, an energetically accessible conical intersection is responsible for the radiationless decay of AIEgens in solution, explaining the observed lack of fluorescence. Theoretical studies using the RACI model have provided detailed mechanistic and dynamic insights.[34–36] Note, however, that in the aggregated state, nonradiative decay pathways are inhibited because the conical intersection is energetically higher than the Franck–Condon (FC) point, or a substantial barrier exists prior to reaching the FC point. Thus, the specific mechanisms by which the AIE process unfolds remain to be fully elucidated. Suzuki and co-workers found that methyl substitution slows the ultrafast internal conversion of benzene from the S_2 to the S_0 state due to the inertia effect, resulting in slower relaxation dynamics and higher quantum yield (QY) for the S_1 state in the order of benzene < toluene < *o*-xylene.[37] Došlić and co-workers showed that methylation of the terminal amide group in NAPMA peptide enhances rigidity, altering the accessibility of the CI seam and affecting non-radiative deactivation.[38] These studies relate the RACI to the significant influence of substituent mass and inertia effects.

Conventional studies on AIE have focused on developing innovative, efficient AIE-active dyes and their utilization in various fields.[39–42] Phenyl-ethylene derivatives, employed as AIE-active dyes, have attracted interest due to their simple molecular structure, adaptability in structural modification, and potential for spectroscopic tuning.[43–46] Recently, the AIE mechanism of similar molecules, such as dimethyl tetraphenylsilole (DMTPS) and diphenyldibenzofulvene (DPDBF), have been explored using surface-hopping molecular dynamics using the RACI model.[28,31,47,48] Cariati *et al.* synthesized and described a prototype compound, 4-dimethylamino-2-benzylidene malonic acid dimethyl ester (Fig. 1).[49] This compound displays lower emissivity in solution or the amorphous phase and significantly higher emissivity in the crystalline phase, demonstrating a crystallization-induced emission. In solution, the excited state transitions barrierlessly to a charge transfer (CT) intermediate due to rotation around the aryl main axis, whereas in the crystalline form, rotation around the aryl main axis is constrained by the crystal packing, leading to minimal geometric relaxation and subsequent radiative decay.[49] Wang *et al.* theoretically deduced that in the molecular state, 4-dimethylamino-2-benzylidene malonic acid dimethyl ester (which they abbreviated as BIM) facilitates the relaxation channel of the β bond (contrary to the experimental observation of aryl rotation around the α bond) around the ethylenic C=C bond, under the CT excitation, as depicted in Fig. 1. This leads to fluorescence quenching *via* a conical intersection near the CT intermediate.[50] However, the computational theory of the highest accuracy (*i.e.*, CASPT2) applied in this study did not identify a conical intersection, leaving unresolved questions about the quenching mechanism. Additionally, the experimental studies by Cariati *et al.*[49] suggest that it is the rotation of the single bond (*i.e.*, the α bond), rather than the double bond (*i.e.*, the β bond), which causes fluorescence quenching.[49] Therefore, the mechanism of fluorescence quenching of BIM in methanol solution has not yet been fully elucidated.

In this study, we explore the AIE mechanism of BIM dye using spin–flip (SF) long-range corrected (LC) time-dependent density functional theory (TDDFT) calculations for the monomer. SF-LC-TDDFT[51,52] is one of the most accurate TDDFT methods, incorporating both long-range exchange and electron correlations associated with double excitations. It is also a fast computational method capable of quantitatively performing excited-state dynamics driven by CT excitations. SF-LC-TDDFT provides highly accurate excitation energies comparable to multireference theory for one-dimensional extended polycyclic

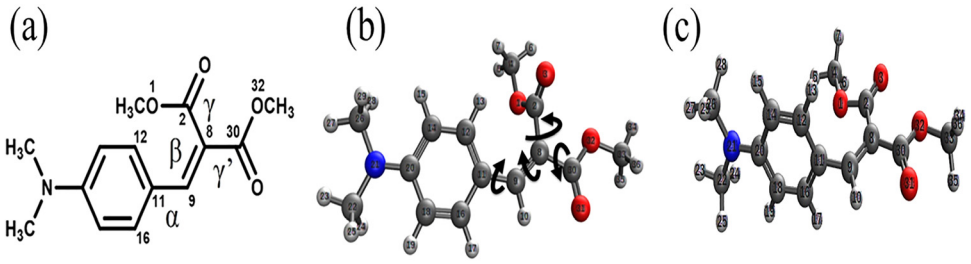

Fig. 1 Chemical structure of (a) 4-dimethylamino-2-benzylidene malonic acid dimethyl ester (BIM) along with the optimized geometries (represented as S_0-MIN and S_1-MIN in this study) of (b) BIM monomer (S_0-MIN) and (c) BIM monomer (S_1-MIN). In (a), the rotating bonds of BIM are defined as the α (12, 11, 9, 8), β (11, 9, 8, 2), γ (9, 8, 2, 1) and γ' (9, 8, 30, 32) dihedral angles. In (b), the directions of rotation of the bonds as the system moves from S_0-MIN to S_1-MIN are shown.

aromatic systems, such as oligoacenes, which exhibit strong double excitation effects.[52] Furthermore, it has been applied to graphene, a two-dimensional extended system with weak double excitation effects, where it successfully reproduced the results of conventional LC-TDDFT.[53] More recently, SF-LC-TDDFT has been utilized to elucidate the triplet generation mechanism in organic photosensitizers.[54,55] We explore the twisted intramolecular charge transfer (TICT) in the BIM monomer and its inhibition in the BIM crystal, quantitatively elucidating the AIE mechanism through SF-LC-TDDFT calculations. LC-TDDFT adequately describes charge-transfer excitations in donor–acceptor type molecules by eliminating long-range self-interaction in the exchange functional, a known limitation of hybrid functionals.[56–59] Therefore, SF-LC-TDDFT is one of the most suitable computational methods for quantitatively elucidating the AIE mechanism of BIM.

2. Computational details

Collinear SF-LC-TDDFT calculations were performed to determine the PES and analytical gradients of both the ground (S_0) and lowest singlet excited (S_1) states of BIM monomer. Due to the specifications of the quantum chemistry software used (Q-Chem 6.1, referred in the next paragraph), the SF-LC-TDDFT calculations were performed using the Tamm–Dancoff approximation. Fig. 1 shows the optimized geometries for both S_0-MIN and S_1-MIN of the monomer. In the collinear SF-LC-TDDFT calculations, spin contamination inevitably occurs. However, the S_0 and S_1 states were identified as the two lowest-energy singlet states, with $\langle S^2 \rangle$ values confirmed to be less than 0.5. Geometry optimization was carried out to determine the equilibrium structure in the S_0 state (S_0-MIN). For the S_1 state, the geometry optimization commenced from the Franck–Condon (FC) point—defined as the geometry where the S_0-MIN is vertically excited to the S_1 state—and proceeded to determine the optimized structure (S_1-MIN). The minimum energy gap (MEG) between the S_0 and S_1 states was determined by checking their energy gap along the minimum energy path (MEP) generated through a PES scan of these states.

For the monomer, electronic structures were calculated using PBE0, B3LYP, BHHLYP, CAM-B3LYP, and ωB97XD functionals with the cc-pVDZ basis sets[60] to check the reliability of these functionals in reproducing experimental observations. All the data are listed in Tables S1 and S2 of the ESI.† ωB97XD[61,62] fully incorporates long-range exchange, allowing it to accurately reproduce charge-transfer excitations in TDDFT calculations. Solvent effects were incorporated using a linear-response conductor-like polarizable continuum model (LR-CPCM) for methanol solution.[63–65] To check the effect of the basis set, we also calculated the S_1 excitation energy using aug-cc-pVDZ and confirmed that it exhibits the same bond angle dependence (as shown in Table S8 of the ESI†). Starting from the corresponding optimized structures constrained geometry optimizations were performed fixing the torsional angle α (see Fig. 1) across a range from 0 to 180° in both the S_0 and S_1 states (Fig. 2a). Furthermore, Fig. 3 illustrates the molecular orbitals corresponding to the main transitions of the S_1 excitation of the BIM molecule at the S_0 and S_1 optimized geometries, highlighting the TICT behavior. All electronic structure calculations were performed using the quantum chemistry software Q-Chem 6.1.[66] To analyze the aggregate state (*i.e.*, the BIM molecular crystal), we extracted a cluster containing 13 molecules from the crystal structure to create the initial setup, as shown in Fig. 4a. Without performing any explicit calculations we manually rotated the α-torsional angle of the central monomer in both clockwise and anti-clockwise directions to examine the intramolecular restrictions within the constrained environment. This analysis helps us to understand why fluorescent quenching pathways are inhibited in the solid state from the perspective of an individual molecule. We constructed the initial arrangement of 13 BIM molecules based on the X-ray crystal data to comprehensively investigate the effects of AIE and gain insights into intermolecular interactions at short distances within the crystal structure. To achieve this, we utilized Mercury software,[67] which allowed us to visualize and

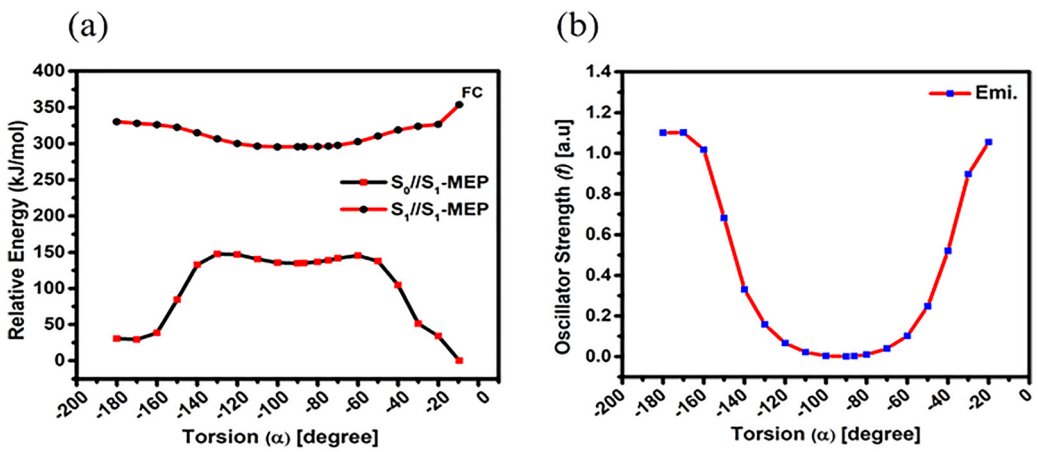

Fig. 2 (a) Potential energy profiles for the S_0 and S_1 states and (b) oscillator strengths of the $S_1 \rightarrow S_0$ de-excitation, calculated for the BIM monomer as a function of the α dihedral angle along the S_1-MEP in methanol solution, using SF-LC-TDDFT with ωB97XD/cc-pVDZ.

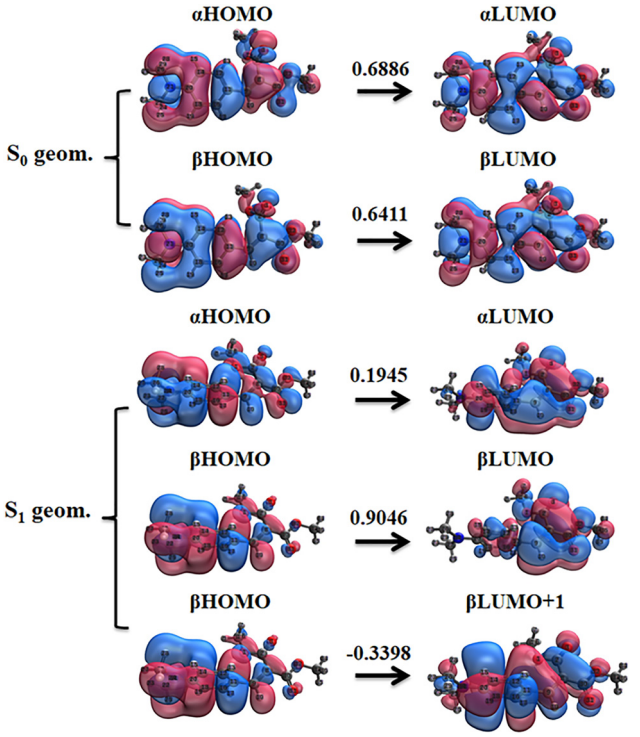

Fig. 3 Molecular orbitals involved in the main transitions of the S_1 excitation of the BIM molecule at the S_0 and S_1 optimized geometries, calculated using SF-LC-TDDFT with ωB97XD/cc-pVDZ. The response coefficients corresponding to each transition are indicated above the arrows.

analyze the intermolecular interactions (described in details in Section 3.3).

3. Results and discussion

3.1. Photophysical property calculations of BIM monomer in methanol

Initially, we conducted SF-TDDFT calculations using the PBE0, B3LYP, BHHLYP, CAM-B3LYP, and ωB97XD functionals on the selected molecule BIM. We compared the computed absorption wavelength values obtained with these different functionals to the reported experimental data for BIM, which indicates a maximum absorption wavelength of 375 nm in a methanol solution. The discrepancies between the calculated values and the experimental data are detailed in Table S2 of the ESI.† Both the B3LYP and PBE0 functionals tended to overestimate the experimental absorption values. In contrast, the ωB97XD, BHHLYP, and CAM-B3LYP functionals yielded nearly identical theoretical absorption values. We have chosen the ωB97XD LC-functional for further study, as it accurately reproduces charge-transfer excitations in TDDFT calculations. Table 1 summarizes the absorption and emission wavelengths for the BIM monomer in methanol solution. The transitions with high oscillator strengths (f) were compared with the reported experimental absorption data. The calculated low $S_0 \rightarrow S_1$ excitation energy of 339 nm, corresponding to the highest oscillator strength f = 1.4169, is reasonably comparable to the experimentally-observed one (375 nm). Moreover, the calculated emission energy of 746 nm at the S_1 optimized geometry, with f = 0.0020, indicates significantly weak emission or almost non-emissive in solution, which aligns with the experimentally reported weak fluorescence. The significant difference between the theoretical and experimental emission wavelengths (747 nm and 464 nm, respectively) can be explained by the experimental finding that the molecule undergoes continuous twisting motion between two extreme geometries around the aryl main axis, *i.e.*, the α bond in Fig. 1. That is, the experimental emission wavelength at 464 nm is almost in the middle of the theoretical absorption (339 nm) and emission wavelengths (747 nm). This will be discussed further in Section 3.2. Additionally, we emphasize that we did not encounter any spin contamination in the SF-LC-TDDFT calculations, which often makes it difficult to differentiate the spin character of excited states. This is evident from the generated values of $\langle S^2 \rangle_{S_0}$ and $\langle S^2 \rangle_{S_1}$ for the S_0 and S_1 optimized geometries, as listed in Table S4 of the ESI.† It is well established in the literature that spin contamination in SF-TDDFT has minimal impact on excitation energies.[68]

Table 2 lists the main transitions, the response coefficients corresponding to each transition, and the excitation energies of the BIM monomer at S_0 and S_1-optimized geometries. As indicated in Table 2, the vertical excitation at 3.66 eV corresponds to the S_1 excitation, which shows a high oscillator strength (see Table 1). The molecular orbitals (MOs) involved in the main transitions of the S_1 excitation at the S_0 and S_1 optimized geometries are displayed in Fig. 3, while the MOs corresponding to the remaining transitions are shown in Fig. S2 of the ESI.†

3.2. Excited state minimum and decay path of BIM monomer in methanol

Based on the above discussion, let us first explore the optimal geometries of the S_0 and S_1 states of the BIM monomer using the PBE0, B3LYP, BHHLYP, CAM-B3LYP, and ωB97XD functionals, focusing on the four main dihedral angles of BIM: α, β, γ, and γ′. As shown in Table S1 of the ESI,† the results for the rotation of the dihedral angles obtained from the B3LYP and PBE0 functionals indicate that the α-bond remains almost stationary, which contradicts experimental findings. In contrast, the ωB97XD, BHHLYP, and CAM-B3LYP functionals demonstrate nearly identical and high rotations of the α-bond. For further investigation, we have chosen the ωB97XD LC-functional. According to Table S3 in the ESI,† the optimized geometry at the S_0 (DFT level) and S_1 (TD-DFT level) does not show any rotation of the α-bond, which contradicts the experimental results. This motivates us to adopt the spin–flip approach and Table 3 summarizes the optimized main angles for the S_0 and S_1 states of the BIM monomer at the SF-TDDFT level. From the table, it can be seen that the difference between the most stable structures of the S_0 and S_1 states of BIM monomer lies in the α and γ angles. As shown in Fig. 1, these are dihedral angles centered

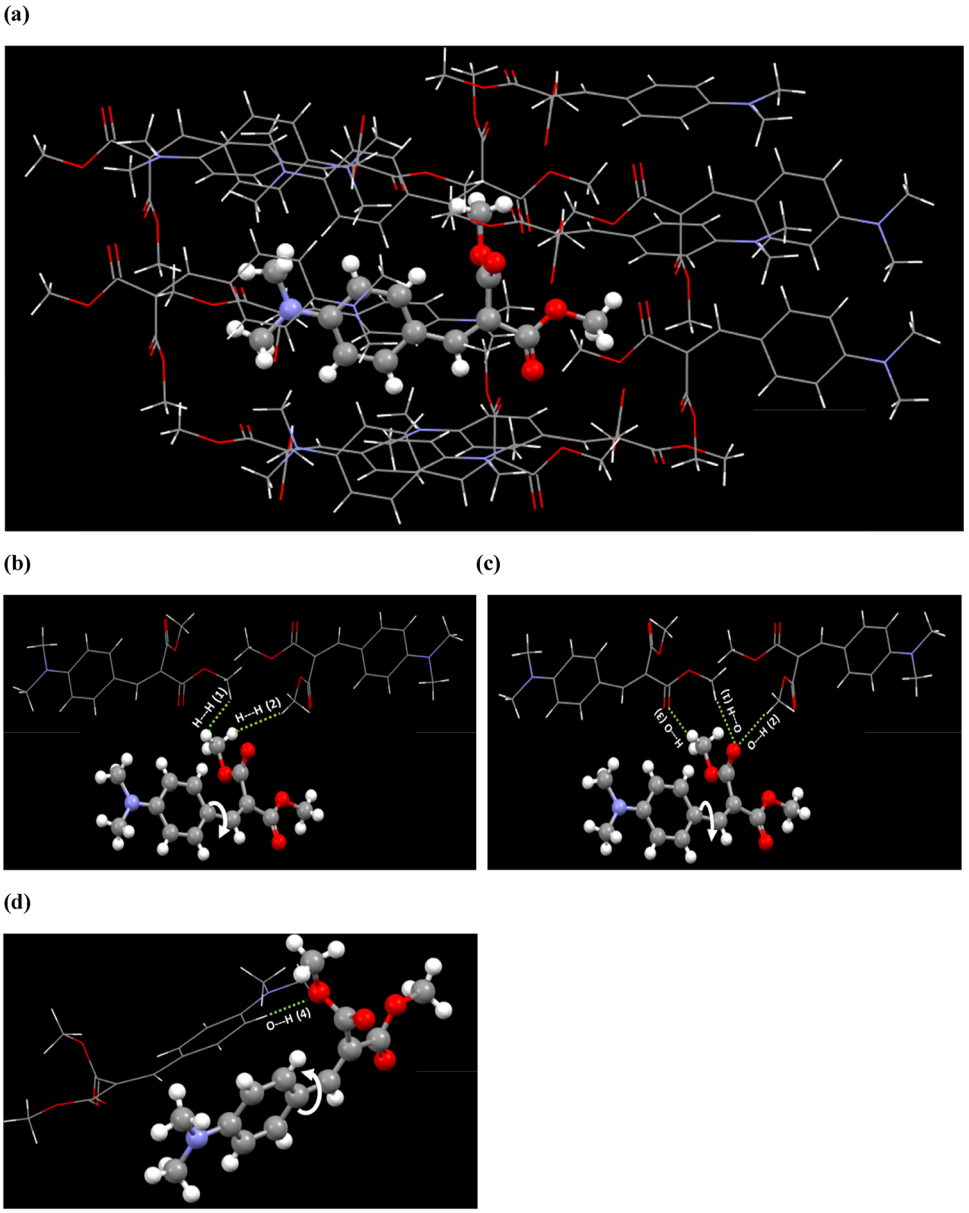

Fig. 4 All the illustrated figures of the crystal structure having $\alpha = -8^{\circ}$ (from crystal file) (a) initial setup of a 13-molecule cluster taken from the crystal structure, the central molecule (ball and stick style), and the surrounding molecules (wireframe style), (b) illustrates the interactions [H···H (1) and H···H (2)] between the central monomer model and the two adjacent monomers when the α-bond rotates in the anti-clockwise direction, (c) short contacts in the crystal structure when the α-bond rotates in the anti-clockwise direction [labeled as O···H (1), O···H (2), and H···O (3)], and (d) short contact in the crystal structure when the α-bond rotates in the clockwise direction [labeled as O···H (4)].

Table 1 Calculated vertical $S_0 \rightarrow S_1$ excitation and $S_1 \rightarrow S_0$ de-excitation energies and the corresponding oscillator strength (f) values for BIM monomer at S_0 and S_1 optimized geometries, respectively. These values were obtained through SF-LC-TDDFT calculations using ωB97XD functional with cc-pVDZ basis set. Corresponding excitation and de-excitation wavelengths are shown in parentheses. Experimental values are provided for comparison

	Vertical excitation at S_0 geometry			Vertical de-excitation at S_1 geometry		
System	Excitation energy	f	Exp.	De-excitation energy	f	Exp.
Monomer	3.66 eV (339 nm)	1.4169	3.31 eV (375 nm)	1.66 eV (747 nm)	0.0020	2.67 eV (464 nm)

around single bonds. For the monomer, the α angle is close to 0° in the S_0 state, while it is close to 90° in the S_1 state. On the other hand, the γ angle is around 65° in the S_0 state and close to 0° in the S_1 state. These results suggest that the $S_0 \rightarrow S_1$ excitation

Table 2 Energy levels of BIM monomer at the S_0 and S_1 optimized geometries, calculated using SF-LC-TDDFT with ωB97XD functional, cc-pVDZ basis sets and LR-CPCM solvent model for methanol. In this table, H and L represent the HOMO and the LUMO, respectively

	SF-LC-TDDFT			
			Excitation energy	
Excited state	Main transitions	Coefficient	(eV)	(nm)
S_0-optimized geometry				
S_0	Ground	0.9887	0	—
T_1	βH → αL	1.0000	2.13	582
T_2	αH → αL	−0.6612	2.60	477
T_2	βH → βL	0.7322		
S_1	αH → αL	0.6886	3.66	339
S_1	βH → βL	0.6411		
S_1-optimized geometry				
S_0	Ground	0.9750	0	—
S_0	βH → βL + 2	−0.1749		
T_1	βH → αL	1.0000	1.00	1240
T_2	αH → αL	0.9533	1.64	756
T_2	βH → βL	−0.1880		
S_1	αH → αL	0.1945	1.66	747
S_1	βH → βL	0.9046		
S_1	βH → βL + 1	−0.3398		

Table 3 Optimized α, β, γ, and γ′ angles of BIM monomer in methanol solution in the S_0 and S_1 states. For the definition of α, β, γ, and γ′ angles, see Fig. 1(a). Geometry optimizations are performed using ωB97XD/cc-pVDZ in the S_0 state and TDωB97XD/cc-pVDZ in the S_1 state

		Angle (°)			
System	State	α	β	γ	γ′
Monomer	S_0	−9.6	−3.2	−65.7	175.1
	S_1	−86.9	−5.7	−6.0	176.5

drives the synchronous rotation of the α and γ angles. Specifically, the α angle rotates from around 0° to around 90°, indicating a high possibility of a complete rotation due to excitation. This also suggests that the synchronous rotation of the α and γ angles is involved in the quenching of the BIM monomer. Cariati *et al.*[49] experimentally demonstrated that the molecule exhibits significantly reduced or even negligible emission in the solution state due to rotation around the *N*,*N*-dimethyl-substituted aryl main axis (*i.e.*, α-bond). This finding was supported by a combination of emission and NMR spectroscopies. In contrast, the molecule exhibits significantly higher emissivity in the crystalline phase, confirming crystallization-induced emission (CIE). The emission of BIM is very weak in solution, with minimal dependence on solvent polarity. However, upon solvent rigidification, the emission is dramatically enhanced. Cariati *et al.* executed the rigidfication by (i) increasing the solvent viscosity from THF to polyethylene glycol-400 (the process is called the 'rigidochromism') and (ii) by lowering the temperature to the solvent's solidification range (207–165 K) (the process is called 'thermochromism'), which minimized geometric relaxation and led to enhanced radiative decay. In the solid-state, however, rotation around the aryl main axis is restricted by crystal packing, allowing the molecule to become emissive. Additionally, a detailed comparison of crystal structures and optical behaviors in the solid-state revealed that J-dimer formation plays a crucial role in the high photoluminescence quantum yield of BIM. The present theoretical results strongly support these experimental findings.

In this context, it is intriguing that the previous theoretical study by Wang *et al.*[50] suggested that the quenching of BIM monomer involves the rotation of the β angle rather than the α angle. They concluded that, based on the optimized main angles in the S_0 and S_1 states, the β bond rotates faster than the α bond, and the potential energy profile of the S_1 state shows that the β bond rotation path is significantly steeper than the α bond one. This results in a more energetically favorable intermediate charge transfer product, indicating that β bond rotation is the predominant S_1 decay path. Thus, the fluorescence quenching of BIM monomer in methanol solution was expected to be caused by β bond rotation due to the narrow S_1–S_0 gap (*i.e.*, MEG) at the intermediate charge transfer product.[50] They did not observe such a steep change in potential energy from the rotation of the α bond, as was claimed in the above-mentioned experimental study.[49] Contrary to this theoretical finding, the optimized main angles of the S_0 and S_1 states in Table 3 suggest that the α bond rotates much faster than the β bond, which aligns well with the experimental study. Based on this result, we calculated the PES of the S_0 and S_1 states along the α bond rotation. Fig. 2(a) illustrates the PESs of the S_0 and S_1 states of the BIM monomer in the methanol solution phase. As shown in the figure, the PES of the S_0 state reaches a maximum value of 148 kJ mol^{-1} when the α angle is 130°. On the other hand, due to torsional rotation around the dihedral α angle, the PES of the S_1 state gradually decreases from the vertically excited Franck–Condon point. The minimum value of the S_1 PES is at α = 100°. The MEG of 153 kJ mol^{-1} is found at α = 120°, between the PESs of the S_0 and S_1 states, as shown in Fig. 2a (see also in Table S7 of the ESI†). The PESs of the S_0 and S_1 of the BIM monomer were also calculated as a function of β bond rotation. Our findings contradict the conclusions of the previous study by Wang *et al.* We observed that the energy difference between the S_0 and S_1 PESs remains significant, and we did not observe any notable energy variations that would indicate a CI. All relevant values are tabulated in Table S9 and Fig. S1 of the ESI.† Further, to gain a deeper understanding of the mechanism, a 2D scan around the α and β torsional angles was conducted. All the energy values of the S_0 and S_1 states are tabulated in Table S10 of the ESI.† The contour plot (illustrated in Fig. S3 of the ESI†) shows that when α is set to 0°, the energy of the S_1 state is minimized at β = 90°. Similarly, when β is at 0°, the lowest energy for the S_1 state occurs at α = 90°. This indicates that when α rotates, β remains constant, and *vice versa*. Therefore, we can conclude that the lowest energy of the S_1 state is achieved when either α or β is rotated by 90°, but not both at the same time.

To clarify how emission changes with the rotation of the α angle in the BIM monomer, we also examine the changes in oscillator strength, which is the dominant factor in the emission transition moment. Fig. 2(b) shows the values of oscillator

Table 4 Intermolecular contact bond distances (in Å) for H···H, O···H, and H···O as the α-torsion angle rotates anti-clockwise

α-torsion angle (°) (anti-clockwise rotation)	Contact bond distance (Å)				
	H···H (1)	H···H (2)	O···H (1)	O···H (2)	H···O (3)
−8	3.2	4.0	2.6	2.5	2.7
0	2.9	3.6	2.6	2.4	2.5
10	2.4	3.2	2.6	2.2	2.4
20	2.1	2.8	2.6	2.2	2.3
30	1.7	2.4	2.7	2.2	2.3
40	1.3	2.0	2.8	2.2	2.3
50	1.0	1.6	3.0	2.4	2.4
60	0.8	1.3	3.2	2.5	2.6

strength in relation to the α angle and all the corresponding values are tabulated in Table S5 of the ESI.† Remarkably, the oscillator strength decreases to near zero around an α angle of 90°. This indicates that significant quenching occurs with the rotation of the α angle. Since the experimental study[49] suggests that the BIM monomer undergoes α bond rotation, this result clearly explains the reason for the experimentally observed quenching of the BIM monomer. This also indicates that BIM is a system that undergoes twisted intramolecular charge transfer (TICT). Fig. 3 displays the molecular orbitals corresponding to the main transitions of the S_1 excitation of BIM molecule at the S_0 and S_1 optimized geometries. From Fig. 3, it can be seen that the BIM monomer has a set of molecular orbitals that give a locally excited transition in the most stable structure at the ground state geometry, whereas in the most stable structure of the S_1 state after α rotation, the BIM monomer has a set of molecular orbitals that indicate a charge transfer transition. This is similar to the excitation observed in DMABN[69] and indicates that the BIM monomer is a typical TICT system.

3.3. Excited state decay path of BIM crystal

Next, we examine the aggregate state of the BIM molecular crystal. According to the RIR model of AIE, restricting intramolecular rotations in an aggregate state effectively suppresses nonradiative decay pathways, leading to enhanced emission.[15–17] In the crystalline phase, BIM's bond rotations are distinct from those in methanol solution, as the steric and electrostatic constraints of the crystalline environment significantly influence molecular behavior. To assess whether the rotation of the α-bond is allowed within the crystal structure, we utilized a 13-molecule cluster containing 468 atoms extracted from the crystal structure to create the initial setup (shown in Fig. 4a). In this model, a single BIM luminophore positioned at the center serves as the model molecule. Only the central BIM molecule is allowed to rotate its α-bond during the analysis, while the surrounding molecules remain fixed. While manually rotating the α-bond of the model BIM monomer may not perfectly replicate the physical behavior of the crystal, it is sufficient to provide insight into why fluorescence quenching pathways are inhibited in the solid state from the perspective of a single molecule.

Fig. 4(b) illustrates the interactions between the central monomer and two adjacent monomers when the α-bond rotates in the anti-clockwise direction. A decrease in the intermolecular distances between the two hydrogen atoms of the rotating molecule and those of the neighboring monomers, referred to as H···H (1) and H···H (2), was observed.[70–72] Specifically, the distances between H···H (1) and H···H (2) decreased from 3.2 Å and 4.0 Å (at α = −8°) to 0.8 Å and 1.3 Å, respectively, when the α dihedral angle was rotated to 60°. The closest distance between two non-bonded atoms is determined by the sum of their van der Waals radii. For instance, the van der Waals radius of a hydrogen atom is 1.2 Å, meaning the closest possible distance between two hydrogen atoms (H···H) is 2.4 Å. Based on this, it is reasonable to conclude that the rotation of the α-bond will likely be restricted near α = 10°, due to steric effects resulting from the rotation. The above process of manual α-bond rotation to some extent mimic the actual constrained optimization because during constrained optimization the surrounding monomers are kept fixed in place as well as the α-angle of the central monomer is constrained while the other internal coordinates of the selected monomer adjust to accommodate the rotation of the α-bond. Consequently, some atoms of the rotating monomer may come into 'short contact' with atoms of neighboring monomers. These short contacts in the crystal structure are defined in Fig. 4(c) and are labeled as O···H (1), O···H (2), and H···O (3). The distances between these atoms are summarized in Table 4. The van der Waals radii for hydrogen and oxygen atoms are 1.2 Å and 1.5 Å, respectively, implying that the minimum permissible distance between H and O atoms (H···O) is 2.7 Å. Therefore, the α-bond rotation is likely to be restricted before or around α = 10°, as evidenced in Table 4.

Following the anti-clockwise rotation, we now focus on the clockwise rotation of the α-bond, as illustrated in Fig. 4(d). The intermolecular distance between the hydrogen and oxygen atoms, labeled as O···H (4), is 2.7 Å at an angle of α = −8°. When the angle is adjusted to α = −10°, this distance decreases to 2.6 Å, and it continues to decrease as the angle moves further from −10°. All the intermolecular distance values are summarized in Table 5. From our observations of clockwise α-bond

Table 5 Intermolecular contact bond distances in Å for O···H as the α-torsion angle rotates clockwise

	α-Torsion angle (°) (clockwise rotation)						
Contact bond distance (Å)	−8	−10	−20	−30	−40	−50	−60
O···H (4)	2.7	2.6	2.4	2.1	1.9	1.6	1.3

rotation, we conclude that the rotation will encounter restrictions at or before $\alpha = -10^{\circ}$, as the minimum permissible intermolecular distance between the hydrogen and oxygen atoms (H···O) is 2.7 Å. With only $\pm 10^{\circ}$ or less α-bond rotation, TICT cannot be achieved in the crystalline state, which strongly inhibits fluorescence quenching. Based on the above discussions, we conclude that the bond rotation relaxation of the BIM molecule, which is observed in solution, is energetically unfavorable in the crystalline phase. As a result, in the aggregate phase, nonradiative decay pathways are significantly suppressed, primarily due to the restriction of intramolecular movements. This restriction leads to enhanced fluorescent quantum yields in the BIM crystal, which explains the AIE phenomena.

4. Conclusions

In this study, the AIE mechanism of the photoluminescent BIM molecule is theoretically explored using SF-LC-TDDFT, the most reliable TDDFT for investigating excited states in medium to large-sized molecules. The PESs of the S_0 and S_1 states of the BIM monomer were calculated for rotation around the main aryl axis (*i.e.*, the torsional angle α). The results revealed that the most stable structure of the S_1 state of the BIM monomer occurs when the α angle is rotated to nearly 90°, consistent with experimental observations that the BIM monomer undergoes rapid α-angle rotation upon photoexcitation. Furthermore, an examination of the changes in oscillator strength with respect to α angle rotation confirmed that it decreases to nearly zero at an α angle of 90°. This finding indicates that the BIM monomer is a TICT system and strongly suggests that quenching in this system is due to a decrease in emission yield caused by α-angle rotation.

Furthermore, the AIE mechanism in the BIM crystal was investigated to understand why fluorescence quenching pathways are inhibited in the solid state (*i.e.*, aggregate state or crystal). By employing a rational approach, without resorting to computationally intensive calculations of the aggregate state, we demonstrated that even a slight rotation of the α-bond (around $\pm 10^{\circ}$ or less) prevents the occurrence of TICT in the crystal structure. Consequently, the bond rotation relaxation of the BIM molecule—the primary mechanism responsible for fluorescence quenching in solution—becomes energetically unfavorable in the crystalline phase. As a result, nonradiative decay pathways are effectively suppressed in the aggregate phase due to restricted intramolecular rotations, leading to a strong inhibition of fluorescence quenching. This restriction significantly enhances the fluorescent quantum yield in the BIM crystal, thereby explaining the aggregation-induced emission (AIE) phenomenon.

Overall, the approach implemented in this work utilizes state-of-the-art excited-state calculations to accurately reproduce photophysical properties and investigate the underlying causes of AIE in BIM, both before and after aggregation. This method offers a powerful tool for analyzing other AIEgens and for the rational design of new photochemical materials. In conclusion, this approach holds significant potential for applications in the field of photochemistry.

Data availability

The data supporting this article have been included as part of the ESI.†

Conflicts of interest

The authors declare no competing financial interest.

Acknowledgements

The authors acknowledge the Department of Chemistry, Birla Institute of Technology and Science (BITS), Pilani, for providing the instrumentation facility. Aarzoo acknowledges BITS-Pilani, Pilani Campus, for research fellowship. R. K. R. acknowledges SERB-DST (Project ref. no. CRG/2023/000285), Government of India, New Delhi as well as JSPS international fellowships for research in Japan for financial support. The authors are also grateful to the computational facilities extended by the High Performance Computation (HPC) center, BITS-Pilani, Pilani Campus. This work was partly supported by the Photo-excitonix Project in Hokkaido University, JST CREST Grant Number JPMJCR1902, JST-Mirai Program Grant Number JPMJMI21EB, and MEXT Program of Data Creation and Utilization-Type Material Research and Development Project Grant Number JPMXP1122712807. A part of the calculations was performed using the Research Center for Computational Science, Okazaki, Japan (Project: 23-IMS-C016, 24-IMS-C017).

References

1 U. Lemmer, S. Heun, R. Mahrt, U. Scherf, M. Hopmeier, U. Siegner, E. Go, K. Mu and H. Ba, *Chem. Phys. Lett.*, 1995, **240**, 373–378.
2 S. W. Thomas, G. D. Joly and T. M. Swager, *Chem. Rev.*, 2007, **107**, 1339–1386.
3 T. Förster and K. Kasper, *Ber. Bunsenges. Phys. Chem.*, 1955, **59**, 976–980.
4 J. Luo, Z. Xie, J. W. Lam, L. Cheng, H. Chen, C. Qiu, H. S. Kwok, X. Zhan, Y. Liu, D. Zhu and B. Z. Tang, *Chem. Commun.*, 2001, 1740–1741.
5 J. Mei, N. L. Leung, R. T. Kwok, J. W. Lam and B. Z. Tang, *Chem. Rev.*, 2015, **115**, 11718–11940.
6 J. Huang, X. Yang, J. Wang, C. Zhong, L. Wang, J. Qin and Z. Li, *J. Mater. Chem.*, 2012, **22**, 2478–2484.
7 W. Z. Yuan, Z. Q. Yu, P. Lu, C. Deng, J. W. Lam, Z. Wang, E. Q. Chen, Y. Ma and B. Z. Tang, *J. Mater. Chem.*, 2012, **22**, 3323–3326.
8 Q. Wan, J. Tong, B. Zhang, Y. Li, Z. Wang and B. Z. Tang, *Adv. Opt. Mater.*, 2020, **8**, 1901520.
9 X. Li, J. Qi, J. Zhu, Y. Jia, Y. Liu, Y. Li and K. Wu, *J. Phys. Chem. Lett.*, 2022, **13**, 9177–9185.
10 M. Wang, G. Zhang, D. Zhang, D. Zhu and B. Z. Tang, *J. Mater. Chem.*, 2010, **20**, 1858–1867.

11 P. Alam, W. He, N. L. Leung, C. Ma, R. T. Kwok, J. W. Lam, H. H. Sung, I. D. Williams, K. S. Wong and B. Z. Tang, *Adv. Funct. Mater.*, 2020, **30**, 1909268.
12 Z. Yang, W. Yin, S. Zhang, I. Shah, B. Zhang, S. Zhang, Z. Li, Z. Lei and H. Ma, *ACS Appl. Bio Mater.*, 2020, **3**, 1187–1196.
13 H. Ma, R. Li, H. Meng, M. Tian, X. Zhang, Y. Liu and Y. Wei, *Small*, 2023, **19**(21), 2204778.
14 T. Zhang, X. Chen, C. Yuan, X. Pang, P. Shangguan, Y. Liu and B. Z. Tang, *Angew. Chem., Int. Ed.*, 2023, **62**, e202211550.
15 J. Chen, C. C. Law, J. W. Lam, Y. Dong, S. M. Lo, I. D. Williams, D. Zhu and B. Z. Tang, *Chem. Mater.*, 2003, **15**, 1535–1546.
16 Z. Yang, W. Qin, N. L. Leung, M. Arseneault, J. W. Lam, G. Liang, H. H. Sung, I. D. Williams and B. Z. Tang, *J. Mater. Chem. C*, 2016, **4**, 99–107.
17 J. Chen, Z. Xie, J. W. Lam, C. C. Law and B. Z. Tang, *Macromolecules*, 2003, **36**, 1108–1117.
18 J. Luo, K. Song, F. L. Gu and Q. Miao, *Chem. Sci.*, 2011, **2**, 2029–2034.
19 N. L. Leung, N. Xie, W. Yuan, Y. Liu, Q. Wu, Q. Peng, Q. Miao, J. W. Lam and B. Z. Tang, *Chem. – Eur. J.*, 2014, **20**, 15349–15353.
20 Y. Ren, J. W. Lam, Y. Dong and B. Z. Tang, *J. Phys. Chem. B*, 2005, **109**, 1135–1140.
21 G. Liang, J. W. Lam, W. Qin, J. Li, N. Xie and B. Z. Tang, *Chem. Commun.*, 2014, **50**, 1725–1727.
22 Q. Zhao, F. Li, S. Liu, M. Yu, Z. Liu, T. Yi and C. Huang, *Inorg. Chem.*, 2008, **47**, 9256–9264.
23 Y. Hong, J. W. Lam and B. Z. Tang, *Chem. Soc. Rev.*, 2011, **40**, 5361–5388.
24 J. Mei, Y. Hong, J. W. Lam, A. Qin, Y. Tang and B. Z. Tang, *Adv. Mater.*, 2014, **26**, 5429–5479.
25 Q. Peng, Y. Yi, Z. Shuai and J. Shao, *J. Am. Chem. Soc.*, 2007, **129**, 9333–9339.
26 S. Yin, Q. Peng, Z. Shuai, W. Fang, Y. H. Wang and Y. Luo, *Phys. Rev. B*, 2006, **73**, 205409.
27 Z. Shuai and Q. Peng, *Nat. Sci. Rev.*, 2017, **4**, 224–239.
28 Q. Li and L. Blancafort, *Chem. Commun.*, 2013, **49**, 5966–5968.
29 R. Crespo-Otero, Q. Li and L. Blancafort, *Chem. Asian J.*, 2019, **14**, 700–714.
30 Y. J. Gao, X. P. Chang, X. Y. Liu, Q. S. Li, G. Cui and W. Thiel, *J. Phys. Chem. A*, 2017, **121**, 2572–2579.
31 X. L. Peng, S. Ruiz-Barragan, Z. S. Li, Q. S. Li and L. Blancafort, *J. Mater. Chem. C*, 2016, **4**, 2802–2810.
32 Y. Shigemitsu, T. Mutai, H. Houjou and K. Araki, *J. Phys. Chem. A*, 2012, **116**, 12041–12048.
33 M. G. Londesborough, J. Dolanský, L. Cerdan, K. Lang, T. Jelínek, J. M. Oliva, D. Hnyk, D. Roca-Sanjuán, A. Francés-Monerris and J. Martinčík, *Adv. Opt. Mater.*, 2017, **5**, 1600694.
34 S. Suzuki, S. Maeda and K. Morokuma, *J. Phys. Chem. A*, 2015, **119**, 11479–11487.
35 G. J. Zhao, K. L. Han, Y. B. Lei and Y. S. Dou, *J. Chem. Phys.*, 2007, **127**, 094307.
36 G. Sun, Y. Zhao and W. Liang, *J. Chem. Theory Comput.*, 2015, **11**, 2257–2267.
37 K. Maeda, A. Boyer, S. Karashima, A. Humeniuk and T. Suzuki, *J. Phys. Chem. Lett.*, 2024, **15**, 11760–11766.
38 M. Mališ, Y. Loquais, E. Gloaguen, C. Jouvet, V. Brenner, M. Mons and N. Došlić, *Phys. Chem. Chem. Phys.*, 2014, **16**, 2285–2288.
39 J. Gierschner, L. Lüer, B. Milián-Medina, D. Oelkrug and H. J. Egelhaaf, *J. Phys. Chem. Lett.*, 2013, **4**, 2686–2697.
40 M. Shellaiah, Y. H. Wu, A. Singh, M. V. R. Raju and H. C. Lin, *J. Mater. Chem. A*, 2013, **1**, 1310–1318.
41 P. Galer, R. C. Korošec, M. Vidmar and B. Šket, *J. Am. Chem. Soc.*, 2014, **136**, 7383–7394.
42 G. F. Zhang, H. Wang, M. P. Aldred, T. Chen, Z. Q. Chen, X. Meng and M. Q. Zhu, *Chem. Mater.*, 2014, **26**, 4433–4446.
43 B. K. An, S. K. Kwon, S. D. Jung and S. Y. Park, *J. Am. Chem. Soc.*, 2002, **124**, 14410–14415.
44 B. K. An, D. S. Lee, J. S. Lee, Y. S. Park, H. S. Song and S. Y. Park, *J. Am. Chem. Soc.*, 2004, **126**, 10232–10233.
45 Z. Song, R. T. Kwok, E. Zhao, Z. He, Y. Hong, J. W. Lam, B. Liu and B. Z. Tang, *ACS App. Mater. Interfaces*, 2014, **6**, 17245–17254.
46 X. Y. Shen, W. Z. Yuan, Y. Liu, Q. Zhao, P. Lu, Y. Ma, I. D. Williams, A. Qin, J. Z. Sun and B. Z. Tang, *J. Phys. Chem. C*, 2012, **116**, 10541–10547.
47 X. Gao, Q. Peng, Y. Niu, D. Wang and Z. Shuai, *Phys. Chem. Chem. Phys.*, 2012, **14**, 14207–14216.
48 A. Prlj, N. Došlić and C. Corminboeuf, *Phys. Chem. Chem. Phys.*, 2016, **18**, 11606–11609.
49 E. Cariati, V. Lanzeni, E. Tordin, R. Ugo, C. Botta, A. G. Schieroni and D. Pasini, *Phys. Chem. Chem. Phys.*, 2011, **13**, 18005–18014.
50 B. Wang, X. Wang, W. Wang and F. Liu, *J. Phys. Chem. C*, 2016, **120**, 21850–21857.
51 Y. A. Bernard, Y. Shao and A. I. Krylov, *J. Chem. Phys.*, 2012, **136**, 204103.
52 T. Tsuneda, R. K. Singh and A. Nakata, *J. Comput. Chem.*, 2016, **37**, 1451–1462.
53 T. Tsuneda, R. K. Singh and A. Nakata, *J. Comput. Chem.*, 2017, **38**, 2020–2029.
54 T. Tsuneda and T. Taketsugu, *Sci. Rep.*, 2022, **12**, 19714.
55 T. Tsuneda and T. Taketsugu, *Sci. Rep.*, 2024, **14**, 829.
56 S. Grimme, *J. Comput. Chem.*, 2006, **27**, 1787–1799.
57 J. Chaudhary, V. Mittal, S. Mishra, A. Daiya, R. Chowdhury, I. R. Laskar and R. K. Roy, *J. Phys. Chem. C*, 2020, **124**, 15406–15417.
58 J. Chaudhary, I. R. Laskar and R. K. Roy, *ACS Appl. Electron. Mater.*, 2022, **4**, 3724–3738.
59 J. Chaudhary, Aarzoo, R. Roy and R. K. Roy, *J. Phys. Chem. A*, 2022, **126**, 5252–5264.
60 T. H. Dunning Jr., *J. Chem. Phys.*, 1989, **90**, 1007–1023.
61 J. D. Chai and M. Head-Gordon, *Chem. Phys.*, 2008, **128**, 084106.
62 J. D. Chai and M. Head-Gordon, *Phys. Chem. Chem. Phys.*, 2008, **10**, 6615–6620.

63 S. Miertuš, E. Scrocco and J. Tomasi, *Chem. Phys.*, 1981, **55**, 117–129.
64 R. Cammi and B. Mennucci, *J. Chem. Phys.*, 1999, **110**, 9877–9886.
65 M. Cossi and V. Barone, *J. Chem. Phys.*, 2001, **115**, 4708–4717.
66 E. Epifanovsky, A. T. Gilbert, X. Feng, J. Lee, Y. Mao, N. Mardirossian and Y. C. Su, *J. Chem. Phys.*, 2021, **155**, 084801.
67 C. F. Macrae, I. Sovago, S. J. Cottrell, P. T. Galek, P. McCabe, E. Pidcock and P. A. Wood, Mercury 4.0, *Appl. Crystallogr.*, 2020, **53**, 226–235.
68 Z. Li, W. Liu, Y. Zhang and B. Suo, *J. Chem. Phys.*, 2011, **134**, 134101.
69 M. Chiba, T. Tsuneda and K. Hirao, *J. Chem. Phys.*, 2007, **126**, 034504.
70 C. F. Matta, J. Hernández-Trujillo, T. H. Tang and R. F. Bader, *Chem. – Eur. J.*, 2003, **9**, 1940–1951.
71 A. Paul, M. Kubicki, C. Jelsch, P. Durand and C. Lecomte, *Acta Crystallogr. B*, 2011, **67**, 365–378.
72 N. K. Monteiro and C. L. Firme, *J. Phys. Chem. A*, 2014, **118**, 1730–1740.

